One-particle-thick, solvent-free, coarse-grained model for biological and biomimetic fluid membranes

Hongyan Yuan,[1] Changjin Huang,[1] Ju Li,[2] George Lykotrafitis,[3] and Sulin Zhang[1,*]
[1]*Department of Engineering Science and Mechanics, Pennsylvania State University, University Park, Pennsylvania 16802, USA*
[2]*Department of Materials Science and Engineering, University of Pennsylvania, Philadelphia, Pennsylvania 19104, USA*
[3]*Department of Mechanical Engineering, University of Connecticut, Storrs, Connecticut 06269, USA*
(Received 18 March 2010; published 12 July 2010)

Biological membranes are involved in numerous intriguing biophysical and biological cellular phenomena of different length scales, ranging from nanoscale raft formation, vesiculation, to microscale shape transformations. With extended length and time scales as compared to atomistic simulations, solvent-free coarse-grained membrane models have been exploited in mesoscopic membrane simulations. In this study, we present a one-particle-thick fluid membrane model, where each particle represents a cluster of lipid molecules. The model features an anisotropic interparticle pair potential with the interaction strength weighed by the relative particle orientations. With the anisotropic pair potential, particles can robustly self-assemble into fluid membranes with experimentally relevant bending rigidity. Despite its simple mathematical form, the model is highly tunable. Three potential parameters separately and effectively control diffusivity, bending rigidity, and spontaneous curvature of the model membrane. As demonstrated by selected examples, our model can naturally simulate dynamics of phase separation in multicomponent membranes and the topological change of fluid vesicles.

DOI: 10.1103/PhysRevE.82.011905 PACS number(s): 82.70.Uv, 87.17.Aa, 81.16.Dn

I. INTRODUCTION

Due to the hydrophobic interactions, amphiphilic molecules in aqueous solutions self-assemble into monolayer (e.g., amphiphilic block copolymers [1]) or bilayer membranes, where rodlike molecules align their longitudinal axes parallel to each other and are able to diffuse laterally at physiologically relevant temperatures. While atomistic simulations [2] have been routinely performed to elucidate physical mechanisms involved in localized lipid organizations, they are inaccessible to many intriguing membrane processes [3,4] that occur on the length scale much larger than membrane thickness. To overcome length and time scale limitations of atomistic simulations, significant efforts have been devoted to develop particle-based coarse-grained models, where each lipid molecule is coarse-grained into several connected beads. In general, particle-based models can simulate membrane fluidity, hydrodynamic effect, and membrane topological changes naturally.

In the explicit-solvent coarse-grained models [5–7], solvent molecules are also coarse grained, i.e., grouping several water molecules into a coarse grain. Explicit-solvent coarse-grained models stabilize membrane in fluid phase by explicitly accounting for the hydrophobic interactions between solvent and lipid particles. While explicit-solvent strategy is convenient and natural, yet it comes with a high computational cost. In coarse-grained simulation settings, membrane particles spread on a two-dimensional (2D) surface, whereas solvent particles occupy the bulk. The solvent degrees of freedom thus vastly outnumber the lipid particles even for a modest sized membrane, limiting the accessible length and time scales of explicit-solvent coarse-grained models.

With the limitations of the explicit-solvent models in mind solvent-free models are highly desired. For solvent-free models in which water molecules are not explicitly modeled, effective intermolecular attractive interactions need to be devised to substitute for the hydrophobic interactions between water molecules and hydrocarbon chains of amphiphilic molecules, which constitutes the major challenge in the development of solvent-free membrane models. Such intermolecular interactions have been successfully developed in chain-of-bead models, where each amphiphilic molecule is coarse grained into a chain of multiple connected beads [8–13]. These chain-of-bead models, e.g., the three-bead model by Cooke and Deserno [11,14,15], have been exploited in mesoscopic membrane simulations.

To push the length and time scales to the highest possible level while retaining key membrane properties, particle-based membrane models, where a single or a cluster of amphiphilic molecules are represented by only one particle, are highly desired. However, attempts to develop such models are often frustrated by the complexity of mimicking the hydrophobic effects in the absence of explicit solvents [4]. In the pioneering model of Drouffe *et al.* [16], particles are able to self-assemble into one-particle-thick fluid phase. However, membrane bending rigidity of this model is significantly lower than the experimental range. In addition, its use of multibody potential complicates the model and increases the computational cost. Along this direction, several other models were proposed, aiming to avoid using multibody potentials or to reproduce experimentally relevant membrane properties [17–19]. In a recent model of such type, Kohyama [19] extended the model of Drouffe *et al.* [16] to a pair potential, where the bending rigidity is controlled by a time-dependent variable. Despite varying degrees of success of these models, it remains unclear whether an anisotropic pair potential as simple as Lennard-Jones (LJ) potential for the

*Corresponding author; suz10@psu.edu

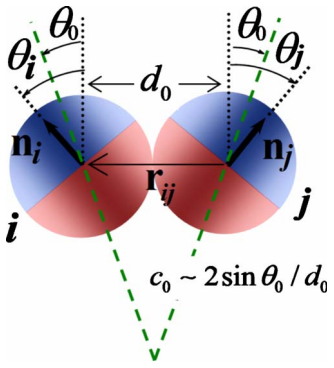

FIG. 1. (Color online) Schematics of the orientation-dependent interparticle interaction. Kinetically, each particle is axisymmetric with a particle-fixed unit vector **n** representing the axis of symmetry, and with mass of m. The interparticle interaction is both distance and orientation dependent. The angle θ_0 is a model parameter charactering the spontaneous curvature. The configuration corresponding to $\theta_i=\theta_j=\theta_0$ is made to be the most energetically favorable relative orientation between two particles. The two halves of each particle are colored distinctly to indicate the orientation of the particle. The spontaneous curvature c_0 is related to θ_0 via $c_0 \sim 2 \sin \theta_0/d_0$, where d_0 is the average interparticle distance.

isotropic case exists to mimic the hydrophobic effect while yielding biologically relevant properties. In addition, for large length scales, triangulated membrane models [20–23] have been intensively used in simulating biological membranes and protein networks [24–26]. The finite element method [27], the meshless method [28], and the phase field approach [29–31] have also been applied to study fluid membranes.

The present work highlights a one-particle-thick fluid membrane model. The interparticle interaction is described by a soft-core pairwise potential, where the interaction strength is dependent on the relative orientations. The pairwise interparticle interaction potential is very simple in its mathematical form but highly tunable, able to robustly self-assemble into fluid membranes with biophysically relevant properties. From length and time scale mappings, each particle in our model represents a few lipid molecules in the lateral direction. Due to its high computational efficiency, our model enables simulations of large-scale membrane topological changes and phase-separation dynamics, as demonstrated by the selected examples.

II. COARSE-GRAINED MODEL

The coarse-grained particles in our model are axisymmetric, with their axes of symmetry representing the longitudinal direction of lipid molecules. The model features a soft-core pairwise interparticle potential with the interaction strength weighed by the relative orientations of the particle pair. Correspondingly, the interparticle potential is constituted of two functions, $u(r)$ and $\phi(\hat{\mathbf{r}}_{ij},\mathbf{n}_i,\mathbf{n}_j)$, which, respectively, describe the distance and orientation dependences. Figure 1 depicts a generic relative position and orientation of such a particle pair, where the two halves of each particle are colored distinctly to indicate its orientation. This coloring scheme facilitates visualization [32] in simulations presented later. We denote $\mathbf{r}_i$ and $\mathbf{r}_j$ the center position vectors of particles i and j, respectively. The interparticle distance vector is then $\mathbf{r}_{ij}=\mathbf{r}_i-\mathbf{r}_j$. We also denote $r=|\mathbf{r}_{ij}|$ and $\hat{\mathbf{r}}_{ij}=\mathbf{r}_{ij}/r$. The unit vectors $\mathbf{n}_i$ and $\mathbf{n}_j$ represent the axes of symmetry of particles i and j, respectively. For simplicity, the rotational degree of freedom about the axis of symmetry of each particle is neglected. Therefore, each particle carries five degrees of freedom, i.e., three translational and two rotational degrees of freedom (noting the constraint $\mathbf{n}\cdot\mathbf{n}=1$).

In searching for the functional form of the distance-dependent function $u(r)$, we found that the classical 12–6 LJ potential only leads to solid membranes at low temperatures and gas phase at high temperatures. Missing of a fluid phase in between is due to the steep energy landscape of the 12–6 LJ potential: the interparticle interaction forces are either too strong (near the equilibrium distance) to permit particle diffusion or too weak (once escaped from the equilibrium distance) to hold particles together. In order to be able to tune the restoring force, we adopt the following two-branch function $u(r)$:

$$u(r)=\begin{cases} u_R(r)=\varepsilon\left[\left(\dfrac{r_{\min}}{r}\right)^4-2\left(\dfrac{r_{\min}}{r}\right)^2\right], & r<r_{\min} \\ u_A(r)=-\varepsilon\cos^{2\zeta}\left[\dfrac{\pi}{2}\dfrac{(r-r_{\min})}{(r_c-r_{\min})}\right], & r_{\min}<r<r_c \end{cases}, \tag{1}$$

where ε and σ are the energy and length units, respectively. The repulsive branch $u_R(r)$ adopts the 4–2 LJ type potential that has a much lower restoring force than the 12–6 LJ potential at the equilibrium distance. The attractive branch $u_A(r)$ is of a cosine function that smoothly decays to zero at the cutoff radius r_c. The exponent ζ tunes the slope of the attractive branch [see Fig. 2(a)] and hence the diffusivity of the particles. The two branches smoothly meet at $r=r_{\min}$ with C^1 continuity. We set the distance at the minimum of the potential $r_{\min}=\sqrt[6]{2}\sigma$, the same as that in the 12–6 LJ potential, and $r_c=2.6\sigma$ to include second-neighbor interactions.

Following the treatment in anisotropic potentials for liquid crystal or colloids [33,34], we use ϕ to weigh the interaction strength for different relative orientations, leading to the final form of the anisotropic pair potential:

$$U(\mathbf{r}_{ij},\mathbf{n}_i,\mathbf{n}_j)=\begin{cases} u_R(r)+[1-\phi(\hat{\mathbf{r}}_{ij},\mathbf{n}_i,\mathbf{n}_j)]\varepsilon, & r<r_{\min} \\ u_A(r)\phi(\hat{\mathbf{r}}_{ij},\mathbf{n}_i,\mathbf{n}_j), & r_{\min}<r<r_c \end{cases}. \tag{2}$$

The orientation-dependent function scales the attractive branch of the distance-dependent potential, while shifts upward the repulsive branch [shown in Fig. 2(b)]. The separate operations ensure a fixed distance of minimum energy for different relative orientations between two particles. The orientation-dependent function substitutes for the hydrophobic effects and takes the following form:

$$\phi=1+\mu[a(\hat{\mathbf{r}}_{ij},\mathbf{n}_i,\mathbf{n}_j)-1], \tag{3}$$

where

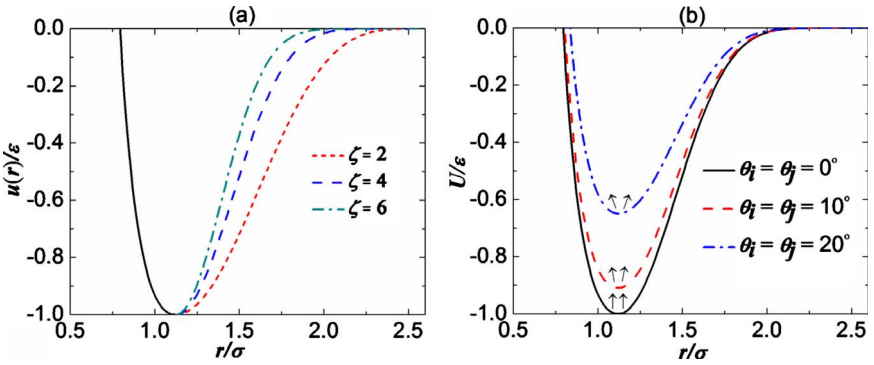

FIG. 2. (Color online) (a) The slope of the attractive branch of the distance-dependent function varies with the exponent ζ. The solid black curve represents the repulsive branch of the function. (b) The interparticle potential U as a function of r for three different θ_i ($\theta_j = \theta_i$) with ζ=4, μ=3, and θ_0=0. The double arrows denote the orientations of a particle pair.

$$a = (\mathbf{n}_i \times \hat{\mathbf{r}}_{ij}) \cdot (\mathbf{n}_j \times \hat{\mathbf{r}}_{ij}) + \sin\,\theta_0(\mathbf{n}_j - \mathbf{n}_i) \cdot \hat{\mathbf{r}}_{ij} - \sin^2\,\theta_0. \tag{4}$$

The function a (hence ϕ) reaches its maximum of 1 when $\theta_i = \theta_j = \theta_0$ (see Fig. 1 for θ_i, θ_j, and θ_0), and is less than 1 otherwise. Hence, the relative orientation $\theta_i = \theta_j = \theta_0$ is most energetically favored. Since θ_0 specifies the favorable interparticle orientations, it directly links to the spontaneous curvature of the model membrane. The parameter μ weighs the energy penalty when the particles are disoriented from θ_0, and is thus related to the bending rigidity of the model membrane.

Corresponding to the two sets of degrees of freedom, particle center positions and orientations, there are two sets of the equations of motion for the coarse-grained model. The first set governs the time evolution of the particle center positions,

$$m_i \ddot{\mathbf{r}}_i = -\frac{\partial U_i}{\partial \mathbf{r}_i}, \tag{5}$$

where m_i is the mass of particle i, $U_i = \Sigma_j U(\mathbf{r}_{ij}, \mathbf{n}_i, \mathbf{n}_j)$, and j runs over all the neighbors of i. The second set of equations governs the time evolution of the particle orientation, which can be derived from Euler's rigid body dynamics equations. However, considering that there are only five degrees of freedom, the equations of motion governing particle orientations can be derived in a more efficient manner. We treat $\mathbf{n}_i$ of particle i as three generalized coordinates with a geometric constraint $\mathbf{n}_i \cdot \mathbf{n}_i = 1$, the governing equations for $\mathbf{n}_i$ can be derived using the Lagrange equations with constraint forces,

$$I_i \ddot{\mathbf{n}}_i = -\frac{\partial U_i}{\partial \mathbf{n}_i} + \lambda_i \mathbf{n}_i, \tag{6}$$

where I_i is the moment of inertia (I_i is fixed to $1 \cdot m_i \sigma^2$ in this work), λ_i is the Lagrange multiplier and has the following relation with $\mathbf{n}_i$ and $\dot{\mathbf{n}}_i$,

$$\lambda_i = \frac{\partial U_i}{\partial \mathbf{n}_i} \cdot \mathbf{n}_i - I_i \dot{\mathbf{n}}_i \cdot \dot{\mathbf{n}}_i. \tag{7}$$

Our coarse-grained molecular dynamics (CGMD) simulations presented below for planar membranes are performed in the $N\Sigma T$ ensemble, where Σ is the membrane tension. Simulations for vesicles are performed in the NVT ensemble. We adopt the Nose-Hoover thermostat [35,36] to maintain the system at desired temperatures. Since our model is solvent-free, the rigid-body translational and rotational motions are removed at each time step in our simulations, which may otherwise cause significant numerical errors. For a planar membrane with periodic boundary conditions, the Berendsen pressure coupling algorithm [37] is modified to a 2D case to maintain a desired tension Σ_0 in the membrane by rescaling the particle coordinates and box size at each time step. The scaling factor χ is

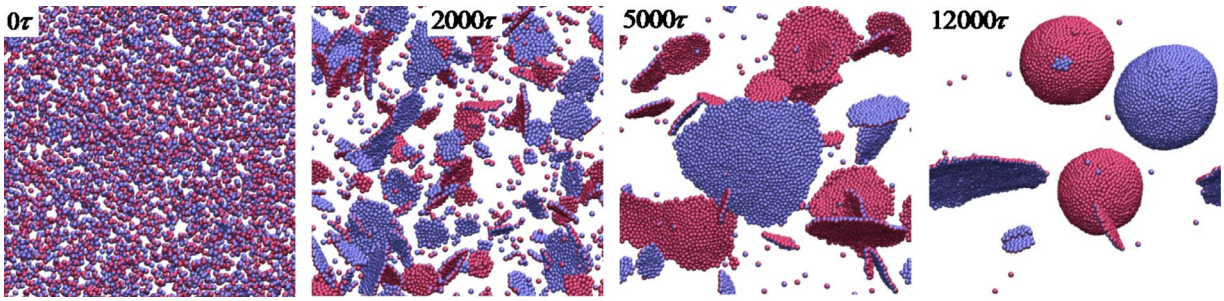

FIG. 3. (Color online) Snapshots from CGMD simulations demonstrating self-assembly of randomly distributed particles into vesicles. The parameters used in the simulations are ζ=4, μ=3, θ_0=0, and $k_B T$=0.17ε.

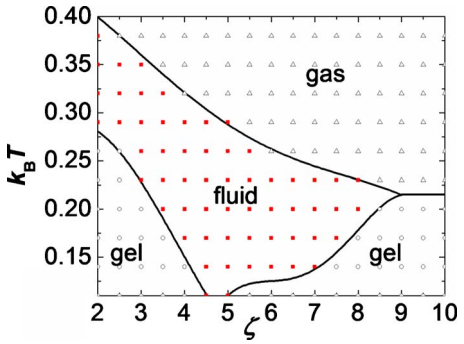

FIG. 4. (Color online) Phase diagram in the (ζ, T) plane at zero tension. Three regions representing gel, fluid, and gas phases are identified, separated by solid lines. A broad fluid phase region with diffusion constant on the order of $0.1\sigma^2/\tau$ exists.

$$\chi = 1 + \frac{\Delta t}{3\tau_p K_A}[\Sigma_0 - \Sigma(t)], \tag{8}$$

where τ_p is the relaxation time, K_A is membrane area compression modulus, Δt is the time step.

III. MEMBRANE PROPERTIES

We next demonstrate that our interparticle potential captures well the hydrophobic interactions and can lead to robust self-assembly of particles into fluid membranes. Starting with a random distribution of 5882 particles enclosed in a cubic box with periodic boundary conditions, CGMD simulations were performed. The particle system is thermostated at a constant temperature of $k_BT=0.17\varepsilon$, with k_B the Boltzmann constant and T the temperature. Figure 3 depicts four simulation snapshots. At intermediate stages ($t=2000\tau$, where $\tau=\sigma\sqrt{m/\varepsilon}$ is the time scale), membrane flakes are formed. The membrane flakes then coalesce into large planar membranes ($t=5000\tau$), and finally close to form vesicles due to the edge effect ($t=12000\tau$). In our simulations, the soft-core interaction potential allows us to adopt a relatively large time step ($\Delta t=0.02\tau$).

We first characterize the diffusion constant as a function of the exponent ζ and temperature T. The preassembled square membrane adopted for this study consists of 5822 particles with side length $\sim 70\sigma$. We maintain zero membrane tension in our simulations and set $\mu=3$ and $\theta_0=0$. The in-plane diffusion constant $D=\langle s_i^2\rangle/4t$ is systematically calculated at zero membrane tension, where s_i is the diffusion distance of particle i over time period t. This allows us to construct a phase diagram of the diffusion constant on the (ζ, T) plane, as shown in Fig. 4. The particle membrane is considered in gel phase if $D<0.01\sigma^2/\tau$, and in gas phase if at least one particle flies away from the membrane during the simulations. We identified a broad fluid phase region in which the diffusion constant is on the order of $0.1\sigma^2/\tau$. The computed diffusion constant is about one order of magnitude higher than the three-bead-chain model [11].

An interesting observation from the phase diagram is that the gel phase occurs at both small and large ζ. We attribute this phasic behavior to the variation of the equilibrium interparticle distance d with ζ due to the second-nearest-neighbor effects. Figure 5(a) (double y-axis) shows that d monotonically increases with ζ, while a maximum of D exists at $d=d_c\sim 1\sigma$. When $d<d_c$, the interparticle interaction is dominated by the repulsive branch of the potential. In this regime, increasing ζ leads to a decrease in the repulsive force between particles, giving rise to a higher diffusivity. On the other hand, when $d>d_c$, the inter-particle interaction is dominated by the attractive branch of the potential. In this regime, increasing ζ leads to an increase in the attractive force, giving rise to a lower diffusivity. In Fig. 5(b), both D and d monotonically increase with temperature and exhibit a sudden rise at $k_BT\sim 0.14\varepsilon$, implying a gel-to-fluid phase transition. The thermal expansion coefficient α_T of the model membrane is fitted at different regimes, as indicated in the figure.

Membrane tension Σ can be calculated by applying the virial formula to the one-particle-thick fluid membranes embedded in three–dimensional (3D) space as,

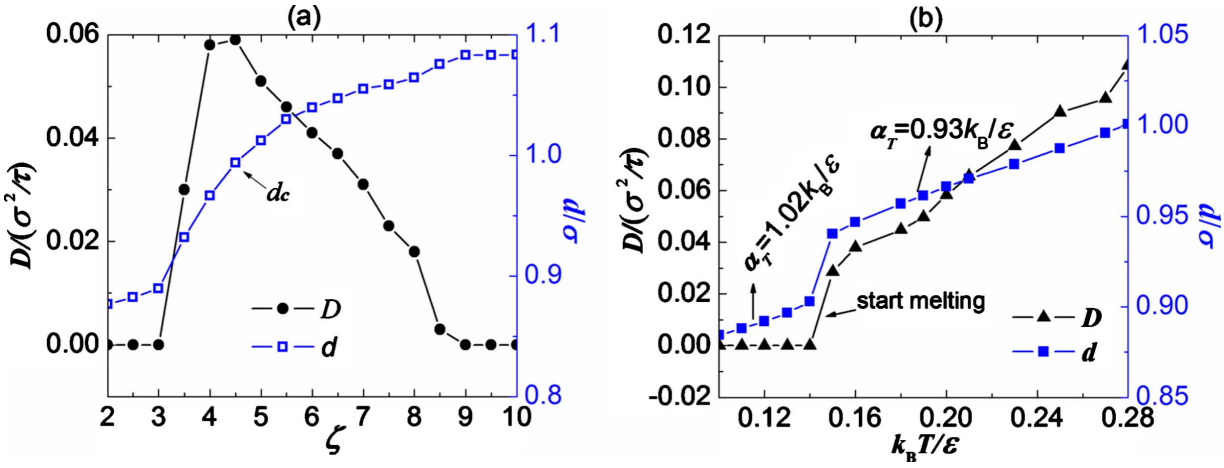

FIG. 5. (Color online) Diffusion constant D and interparticle distance d as functions of the exponent $\zeta(k_BT=0.2\varepsilon)$ (a) and temperature (b) for tensionless membranes. The thermal expansion coefficient α_T of the membrane at different temperature ranges is fitted and indicated in (b).

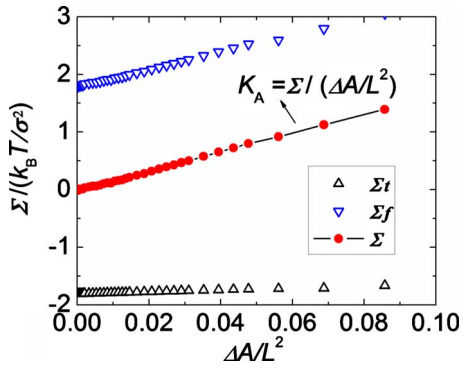

FIG. 6. (Color online) Membrane tension as a function of area strain $\Delta A/L^2$. Area compression modulus K_A is fitted to be about $18k_BT/\sigma^2$. The parameters used in the simulations are $\zeta=4$, $\mu=3$, $\theta_0=0$, and $k_BT=0.23\varepsilon$.

$$\Sigma = -\frac{3Nk_BT}{2A} - \frac{1}{2A}\sum_{i,j>i}^{N} \mathbf{r}_{ij}\cdot\mathbf{F}_{ij}, \tag{9}$$

where A is the membrane contour area, $\mathbf{F}_{ij}$ is the force exerted on particle i by j. The first term on the right-hand side of Eq. (9), denoted by Σ_t, is the kinetic contribution, while the second term, denoted by Σ_f, is the potential contribution. The correctness of Eq. (9) deserves some discussion here. First, considering that a small one-particle-thick membrane patch is locally flat, the out-of-plane stress components only due to the interparticle forces are negligibly small because $\mathbf{r}_{ij}$ and $\mathbf{F}_{ij}$ are almost in-plane vectors. Therefore, the coefficient of Σ_f is set to 1/2. Second, for a fluid membrane in equilibrium, membrane tension is constant everywhere. Therefore, the scalar tension calculated in Eq. (9) around each particle can be summed and averaged over the whole membranes even for curved shapes. Third, the coefficient of 3/2 of term Σ_t comes from the fact that velocity components in all directions contribute to expanding membrane area. Figure 6 plots the kinetic and potential contributions and the total membrane tension as a function of the imposed area strain $\Theta_A = \Delta A/L^2$. The simulations were based on a square membrane of side length $L\sim 140\sigma$. At a critical area strain of ~ 0.09, membrane pore appears. This critical area strain agrees well with experimental data [38]. The kinetic and potential contributions to the membrane tension are on the same order of magnitude, suggesting that neglecting the kinetic term would lead to misinterpretation of membrane tension. The resulting membrane tension is positive, and nearly linearly scales with the imposed area strain. The slope of the tension-strain curve in the large area strain regime corresponds to the area compression modulus, $K_A=\Sigma/\Theta_A$. A linear fitting of the curve yields $K_A\sim 18k_BT/\sigma^2$.

In the continuum limit, the fluctuation spectrum of a square planar membrane of side length L subjected to lateral tension Σ takes the form [39],

$$\langle h_q^2\rangle = \frac{k_BT}{L^2(Bq^4+\Sigma q^2)}, \tag{10}$$

where B is bending rigidity, q is wave number. The simulated fluctuation spectra of a square membrane (consists of 23595 particles) of side length $L\sim 140\sigma$ at zero and finite tensions were given in Fig. 7(a). The q^{-4} dependence of the fluctuation spectrum under zero tension is well predicted. At a finite membrane tension, there exists a critical wave number $q_c=\sqrt{\Sigma/B}$ below which the fluctuation amplitude starts deviating from the zero-tension curve and exhibits a clear q^{-2} dependence. Linear fitting of these two curves at zero and finite membrane tensions yields the bending rigidity and membrane tension, respectively. The fitted membrane tension is $\sim 10\%$ different from the imposed membrane tension. Corresponding to the wavelength of $\sim 8\sigma$, there exists an upper limit of $q=q_m$ beyond which Eq. (10) no longer holds. Both q_c and q_m are marked in Fig. 7(a).

The parametric dependence of bending rigidity on μ is shown in Fig. 7(b), where the bending rigidity is fitted at zero-tension simulations. The bending rigidity monotonically increases with μ. For μ in the range of 2.4–6, the obtained bending rigidity ranges from $\sim 12k_BT$ to $\sim 40k_BT$, which falls in the range of experimental data. There exists a thresh-

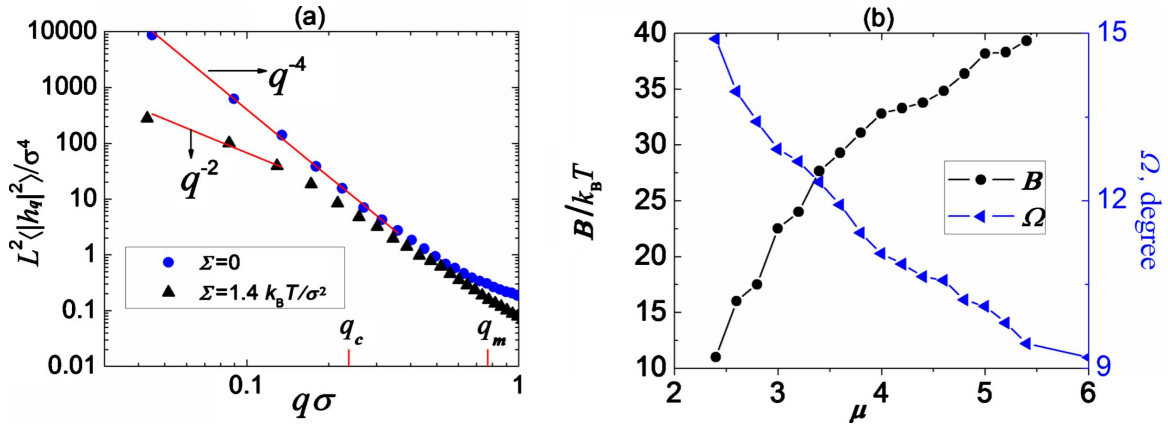

FIG. 7. (Color online) (a) Fluctuation spectra under zero and finite tensions for planar membranes. Both q^{-4} and q^{-2} dependences are well predicted in simulations. The parameters used in the simulations are $\zeta=4$, $\mu=3$, $\theta_0=0$, and $k_BT=0.23\varepsilon$. (b) Membrane bending rigidity (in zero-tension states) monotonically increases with μ, while the order of alignment of the axis of symmetry of particles monotonically decreases with μ. The parameters used in the simulations are $\zeta=4$, $\theta_0=0$, and $k_BT=0.23\varepsilon$.

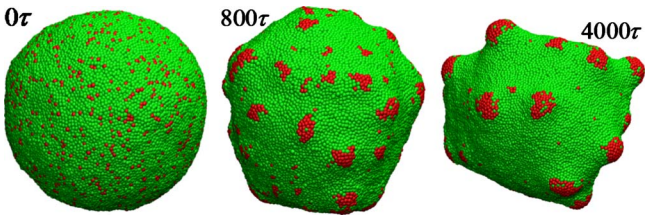

FIG. 8. (Color online) Spontaneous curvature mediated phase separation and subsequent budding.

old value of μ below which the membrane loses its integrity due to the weak orientation preference. The parameter μ also governs the order of alignment of particle-fixed vector $\mathbf{n}$, characterized by the average angle $\Omega=\cos^{-1}(\langle \mathbf{n}_i \cdot \mathbf{e}_z \rangle)$, where $\mathbf{e}_z$ is the normal direction of the reference plane. As shown in Fig. 7(b), Ω ranges from about 9° to 15°, and decreases with increasing bending rigidity.

Due to the orientation dependence of the interparticle potential, the inter-particle interaction depends on the direction along which two particles approach each other, which indicates that the particle is geometrically anisotropic. The aspect ratio can be deduced from the bending and area compression moduli. For a thin structureless plate with vanishing two-dimensional shear modulus, $B=K_A d_{th}^2/12$ holds [40], where d_{th} is the plate thickness. Taking $K_A \sim 18 k_B T/\sigma^2$ and $B \sim 20 k_B T$, the particle aspect ratio of this model is found to be $d_{th}/\sigma \sim 3.7$. The thickness of bilayer membrane is $d_{th} \sim 5$ nm, which specifies the length scale of our model $\sigma \sim 1.4$ nm as far as a bilayer membrane is concerned. Given that a single lipid molecule occupies an area of ~ 0.5 nm^2, each particle in our membrane model represents a few lipids in the lateral direction. A typical value for the diffusion constant of lipids in real phospholipid membranes is about 1 μm^2/s [41]. The diffusion constant of our model is $\sim 0.1\sigma^2/\tau$, which maps out the time scale of our model $\tau \sim 0.1$ μs. Both the length and time scales are about one order of magnitude higher than the chain-of-bead coarse-grained model [11]. Here, the length scale comparison is based on the fact that each particle in our model represents a few lipids in two leaflets of the bilayer. So the degrees of freedom involved in the same membrane area are about one order of magnitude fewer than the chain-of-bead models.

We next demonstrate the applicability of our model by selected examples. For bilayer membranes, "effective" spontaneous curvature may originate from molecule asymmetry [42], area mismatch between two leaflets [43] of the bilayer, or protein-lipid hydrophobic mismatch, or protein-assisted curvatures [14,44]. Spontaneous curvature plays a critical role in determining shape transformations in vesicles and red blood cells [45,46], and is also thought to be related to lipid-sorting in biological membranes [47]. Figure 8 demonstrates phase separation in a binary lipid membrane. The number ratio of the particle types A (red) and B (green) is 1:10. We assign different θ_0 and μ to the different combinations of particle pairs, i.e., $\theta_0^{AA}=\theta_0^{AB}=11.5°$, $\theta_0^{BB}=0°$, $\mu^{AA}=\mu^{AB}=6$, and $\mu^{BB}=3$. Other parameters used in the simulations are: $k_B T=0.23\varepsilon$, $\zeta=4$. It should be noted that different spontaneous curvatures of the two species result in a line tension that induces the phase separation. Starting from random mixture of the particle species, our CGMD simulations show that the two lipid species demix rapidly, forming small domains ($t=800\tau$). The small domains gradually grow into stable domains of roughly the same size ($t=4000\tau$). Further coalescence of neighboring domains seems to be inhibited due to the membrane-mediated elastic interaction [48].

Figure 9 shows four snapshots of our simulations of adhesion-driven endocytosis of nanoparticles (NP) (red). The interaction between the NP and the membrane particles is nonspecific and described by the 4–2 LJ potential with a cutoff of 3.0σ. The parameters for membrane particles are: $k_B T=0.23\varepsilon$, $\zeta=4$, $\mu=3.0$, and $\theta_0=0°$. The energy depth of the 4–2 LJ potential is ε, corresponding to $\sim 4.4 k_B T$. The total resulting adhesion energy (depending on the number of membrane particles that adhere to the NP) is sufficient to overcome the bending energy penalty ($8\pi B$) and drive NP endocytosis [49–51]. The membrane particles in blue are within the interaction range of the NP. For the clarity of visualization, the front half of the membrane model is not shown. The snapshots show the sequence of endocytosis of the NP (from left to right): docking, partial wrapping, pinching off. The NP is then internalized, while acquiring a layer of membrane particles.

IV. CONCLUSION

In conclusion, we have developed a particle-based solvent-free fluid membrane model. Several unique features are attributed to the success of this model. First, the simple mathematical form of the interparticle pair potential and the one-particle-thick coarse-graining substantially improve the accessible length and time scales. The great computational efficiency enables the model to simulate a broad range of membrane processes that occur at microscopic scale. Second, the pair potential is highly tunable and faithfully reproduces biologically relevant membrane properties. The three model parameters independently and effectively control diffusion constant, bending rigidity, and spontaneous curvature, respectively. Due to the particle-based nature, our model simu-

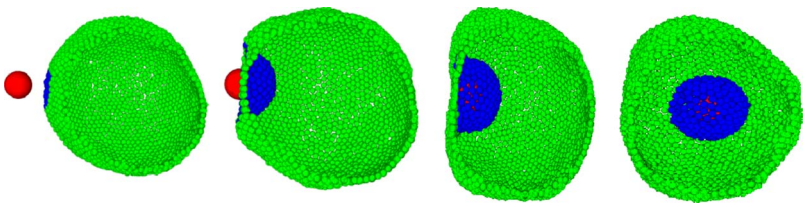

FIG. 9. (Color online) Simulation snapshots of nanoparticle endocytosis.

lates molecular diffusion, fluidity and topological changes of membranes naturally.

Over past decades, considerable attention has been paid to simulate vesicle-substrate interactions and interpret experimentally measured membrane fluctuations of human red blood cells (RBC) at normal or disease states [52–55]. Theoretical analysis of membrane fluctuations has been mainly limited to planar membranes [53] or quasispherical vesicles [56]. Triangulated Monte Carlo membrane models have been used to simulate fluid membrane fluctuations [23], where "fluidity" is realized by dynamic bond flipping. The chain-of-bead models are typically inaccessible to long-wavelength modes. As previously demonstrated, our model faithfully reproduces fluctuation spectrum at zero and finite tension. Therefore, it stands as an ideal model for studying fluctuations of membranes in gel or fluid phase, or membrane fluctuations constrained by substrate or coupled to protein network [55].

Presented elsewhere [57], we have established an efficient algorithm for controlling the volume of a vesicle constituted by the particles. Reducing the vesicle volume using this algorithm enables a series of vesicle shape transformations. Combining our one-particle-thick membrane model with the volume-control algorithm thus enables studies of fluctuation of non-spherical vesicles.

It has been long unclear whether a one-particle-thick membrane model with compatible membrane properties can be established using a simple anisotropic pair potential. Being as simple as LJ potential, our model for the first time provides a conclusive answer. We attribute the success of our model to two aspects: soft-core repulsive and attractive interactions and a strongly biased relative orientation between a particle pair. The unique combination of the simple mathematical form and its comprehensive capabilities in simulating 2D fluid membrane physics can help understand fundamental aspects of soft condensed matter physics of fluid membranes.

ACKNOWLEDGMENTS

SLZ acknowledges the support from National Science Foundation under Awards No. 0826841 and No. 0600642. JL acknowledges the support by NSF DMR–0520020 and AFOSR FA9550–08–1–0325.

[1] L. F. Zhang, K. Yu, and A. Eisenberg, Science **272**, 1777 (1996).
[2] R. R. Gullapalli, M. C. Demirel, and P. J. Butler, Phys. Chem. Chem. Phys. **10**, 3548 (2008).
[3] M. Deserno, Macromol. Rapid Commun. **30**, 752 (2009).
[4] H. Noguchi, J. Phys. Soc. Jpn. **78**, 041007 (2009).
[5] R. Goetz and R. Lipowsky, J. Chem. Phys. **108**, 7397 (1998).
[6] M. Laradji and P. B. Sunil Kumar, Phys. Rev. Lett. **93**, 198105 (2004).
[7] S. Yamamoto and S. Hyodo, J. Chem. Phys. **118**, 7937 (2003).
[8] H. Noguchi and M. Takasu, Phys. Rev. E **64**, 041913 (2001).
[9] O. Farago, J. Chem. Phys. **119**, 596 (2003).
[10] Z. J. Wang and D. Frenkel, J. Chem. Phys. **122**, 234711 (2005).
[11] I. R. Cooke and M. Deserno, J. Chem. Phys. **123**, 224710 (2005).
[12] G. Brannigan, P. F. Philips, and F. L. H. Brown, Phys. Rev. E **72**, 011915 (2005).
[13] J. D. Revalee, M. Laradji, and P. B. S. Kumar, J. Chem. Phys. **128**, 035102 (2008).
[14] B. J. Reynwar *et al.*, Nature (London) **447**, 461 (2007).
[15] I. R. Cooke, K. Kremer, and M. Deserno, Phys. Rev. E **72**, 011506 (2005).
[16] J. M. Drouffe, A. C. Maggs, and S. Leibler, Science **254**, 1353 (1991).
[17] G. Brannigan and F. L. H. Brown, J. Chem. Phys. **120**, 1059 (2004).
[18] P. Ballone and M. G. Del Popolo, Phys. Rev. E **73**, 031404 (2006).
[19] T. Kohyama, Physica A **388**, 3334 (2009).
[20] H. Noguchi and G. Gompper, Proc. Natl. Acad. Sci. U.S.A. **102**, 14159 (2005).
[21] E. Atilgan and S. X. Sun, J. Chem. Phys. **126**, 095102 (2007).
[22] G. Gompper and D. M. Kroll, J. Phys.: Condens. Matter **9**, 8795 (1997).
[23] H. G. Dobereiner *et al.*, Phys. Rev. Lett. **91**, 048301 (2003).
[24] J. Li *et al.*, Biophys. J. **88**, 3707 (2005).
[25] M. Dao, J. Li, and S. Suresh, Mater. Sci. Eng., C **26**, 1232 (2006).
[26] J. Li *et al.*, Proc. Natl. Acad. Sci. U.S.A. **104**, 4937 (2007).
[27] F. Feng and W. S. Klug, J. Comput. Phys. **220**, 394 (2006).
[28] H. Noguchi and G. Gompper, Phys. Rev. E **73**, 021903 (2006).
[29] L. T. Gao, X. Q. Feng, and H. J. Gao, J. Comput. Phys. **228**, 4162 (2009).
[30] T. Biben, K. Kassner, and C. Misbah, Phys. Rev. E **72**, 041921 (2005).
[31] Q. Du, C. Liu, and X. Q. Wang, J. Comput. Phys. **198**, 450 (2004).
[32] W. Humphrey, A. Dalke, and K. Schulten, J. Mol. Graphics **14**, 33 (1996).
[33] J. G. Gay and B. J. Berne, J. Chem. Phys. **74**, 3316 (1981).
[34] R. Everaers and M. R. Ejtehadi, Phys. Rev. E **67**, 041710 (2003).
[35] S. Nose, Mol. Phys. **52**, 255 (1984).
[36] W. G. Hoover, Phys. Rev. A **31**, 1695 (1985).
[37] H. J. C. Berendsen *et al.*, J. Chem. Phys. **81**, 3684 (1984).
[38] R. Lipowsky and E. Sackmann, *Structure and Dynamics of Membranes* (Elsevier Science, Amesterdam, 1995), Vol. 1 and 2.
[39] F. Brochard and J. F. Lennon, J. Phys. (Paris) **36**, 1035 (1975).
[40] R. Goetz, G. Gompper, and R. Lipowsky, Phys. Rev. Lett. **82**, 221 (1999).
[41] P. F. Fahey and W. W. Webb, Biochemistry **17**, 3046 (1978).
[42] W. Helfrich, Z. Naturforsch C **28**, 693 (1973).
[43] M. P. Sheetz and S. J. Singer, Proc. Natl. Acad. Sci. U.S.A. **71**, 4457 (1974).

[44] P. D. Blood and G. A. Voth, Proc. Natl. Acad. Sci. U.S.A. **103**, 15068 (2006).
[45] H. W. G. Lim, M. Wortis, and R. Mukhopadhyay, Proc. Natl. Acad. Sci. U.S.A. **99**, 16766 (2002).
[46] U. Seifert, Adv. Phys. **46**, 13 (1997).
[47] U. Seifert, Phys. Rev. Lett. **70**, 1335 (1993).
[48] T. S. Ursell, W. S. Klug, and R. Phillips, Proc. Natl. Acad. Sci. U.S.A. **106**, 13301 (2009).
[49] H. Y. Yuan and S. L. Zhang, Appl. Phys. Lett. **96**, 033704 (2010).
[50] S. L. Zhang *et al.*, Adv. Mater. **21**, 419 (2009).
[51] M. Deserno and T. Bickel, EPL **62**, 767 (2003).
[52] H. Strey and M. Peterson, Biophys. J. **69**, 478 (1995).
[53] T. Auth, S. A. Safran, and N. S. Gov, Phys. Rev. E **76**, 051910 (2007).
[54] Y. Park *et al.*, Proc. Natl. Acad. Sci. U.S.A. **107**, 1289 (2010).
[55] Y. K. Park *et al.*, Proc. Natl. Acad. Sci. U.S.A. **105**, 13730 (2008).
[56] S. T. Milner and S. A. Safran, Phys. Rev. A **36**, 4371 (1987).
[57] H. Yuan, C. Huang, and S. Zhang, Soft Matter (to be published).